Biomaterials Science

ROYAL SOCIETY OF CHEMISTRY

PAPER

View Article Online
View Journal | View Issue

Cite this: *Biomater. Sci.*, 2025, **13**, 2115

In vitro and *in vivo* degradation studies of a dual medical-grade scaffold design for guided soft tissue regeneration†

Mina Mohseni,[a,b] Silvia Cometta,[a,c] Leopold Klein,[a,d] Marie-Luise Wille,[a,c] Cedryck Vaquette,[e] Dietmar W. Hutmacher *[a,b,c] and Flavia Medeiros Savi*[a,c]

Biodegradable scaffolds with tailored mechanical and structural properties are essential for scaffold-guided soft tissue regeneration (SGSTR). SGSTR requires scaffolds with controllable degradation and erosion characteristics to maintain mechanical and structural integrity and strength for at least four to six months. Additionally, these scaffolds must allow for porosity expansion to create space for the growing tissue and exhibit increased mechanical compliance to match the properties of the newly formed tissue. Although progress has been made in this area, previous studies have yet to fully explore these aspects using biodegradable polymers that are synthesized and 3D printed into filaments classified as medical-grade. In this study, we optimized scaffold design based on the properties of biodegradable materials and employed digital-assisted 3D printing to adjust the degradation pathway of dual-material scaffolds dynamically, thereby modulating mechanical and structural changes. Two medical-grade 3D printing filaments were utilized: Dioxaprene® (DIO), which has a degradation rate of approximately six months, and Caproprene™ (CAP), which has a degradation rate of about 36 months. The scaffolds were 3D printed with these materials to create the desired architecture. An *in vitro* degradation study showed the increasing pore size and compliance (>90% increase) of the scaffold architecture *via* the breakdown of DIO. Meanwhile, the slow-degrading CAP maintained long-term mechanical and structural integrity. Furthermore, over six months of subcutaneous implantation in rats, the dual material showed an approximately two-fold increase in mechanical compliance and free volume expansion, with the pore size increasing from 1 mm to 2 mm to accommodate the growing tissue. The scaffold remained structurally intact and provided mechanical support for the newly formed tissue. Histological and immunohistochemical analyses indicated good *in vivo* biocompatibility, tissue guidance, and the formation of organized soft tissue architecture, supported by an extensive network of blood vessels.

Received 27th August 2024,
Accepted 5th December 2024

DOI: 10.1039/d4bm01132e

rsc.li/biomaterials-science

Introduction

A central requirement for scaffold-guided soft tissue regeneration (SGSTR) is a tailored scaffold design based on the convergence of required material properties and morphology for the targeted soft tissue of a specific organ (skin, breast, liver, *etc.*). Materials used for SGSTR should be able to undergo dynamic changes in their mechanical and structural properties throughout the tissue regeneration process to maintain continuous biomechanical and biochemical functionality. During the initial stages of regeneration, a highly porous and interconnected architecture is recommended to orchestrate blood clot and hematoma formation inside and outside the scaffold. As tissue regeneration and remodelling proceed, larger blood vessels develop to provide functional anastomoses with the host tissue. At later stages of regeneration, a degrading porous structure, which is losing mass but still mechanically supportive, is needed to provide larger pore space for the growing tissue and avoid promoting a myofibroblast phenotype that would result in fibrous encapsulation of the scaffold. The long-term mechanical stability of the degrading scaffold is essential to minimize load transfer to

[a]*Regenerative Medicine Group, School of Mechanical, Medical and Process Engineering, Queensland University of Technology, Brisbane, QLD 4000, Australia. E-mail: dietmar.hutmacher@qut.edu.au*
[b]*ARC Training Centre for Cell and Tissue Engineering Technologies, Queensland University of Technology, Brisbane, QLD 4000, Australia*
[c]*Max Planck Queensland Centre for the Materials Science of Extracellular Matrices, Queensland University of Technology, Brisbane, QLD 4000, Australia*
[d]*Institute of Biomedical Engineering, Department for Medical Technologies and Regenerative Medicine, Eberhard Karls University Tübingen, Tübingen, Germany*
[e]*School of Dentistry, The University of Queensland, Herston, QLD, 4001, Australia*
† Electronic supplementary information (ESI) available. See DOI: https://doi.org/10.1039/d4bm01132e

the newly formed soft tissue until subsequent remodelling stages. Otherwise, at the cellular level, excessive stress and strain inhibit cell proliferation and differentiation, and at the tissue level, the lack of a physical substrate to withstand external loads leads to incomplete, inadequate and compromised regeneration. Moreover, multi-material scaffolds with long-term mechanical and structural integrity resist changes in shape caused by external forces and from cellular and tissue ingrowth and subsequently facilitate the guidance of the growing tissue towards complex anatomical shapes, especially in the case of large tissue defects where greater biomechanical forces exist.[1,2]

Taken collectively, a scaffold should have the following properties: (1) mechanical properties able to withstand biomechanical loading at the host site, (2) the capacity for expansion to generate free space for new tissue formation after the first tissue remodelling phase, (3) increasing mechanical compliance compatible with the newly formed tissue, and (4) a tailored bioerosion pathway of the biodegradable polymer to modulate local degradation profiles and dynamically control these mechanical and structural changes across the entire tissue regeneration process. For SGSTR scaffolds, this prerequisite has yet to be holistically addressed through a single workflow using medical-grade materials, especially for large-scale regeneration where complex inter-scale relations exist between mechanics, biology and topology.

Since scaffold degradation results from interactions between bulk material properties, structural architecture and the physiological environment, variation in the local degradation profile of single-material scaffolds is challenging compared to composite structures.[3] One approach to overcome this problem is to control the spatial placement of different materials in composite structures in conjunction with well-understood material properties and rational design strategies to facilitate modulating the overall degradation profile (Fig. 1). The combination of fast-degrading and slow-degrading polymers in fixed ratios allows precise tailoring of the overall degradation of the composite.[4] Regarding the complexity of composite structures, additive manufacturing (AM) offers a unique level of control to position materials in a pre-designed pattern that would otherwise be time-consuming and technically challenging using conventional manufacturing techniques.[5–8] With the advent of AM multi-nozzle systems and toolpath planning, the spatial placement of different biodegradable polymers can be independently tuned to achieve a multi-material scaffold design.[9–12]

In this study, a platform of material, design, and fabrication is developed to control the erosion pathway of composite struc-

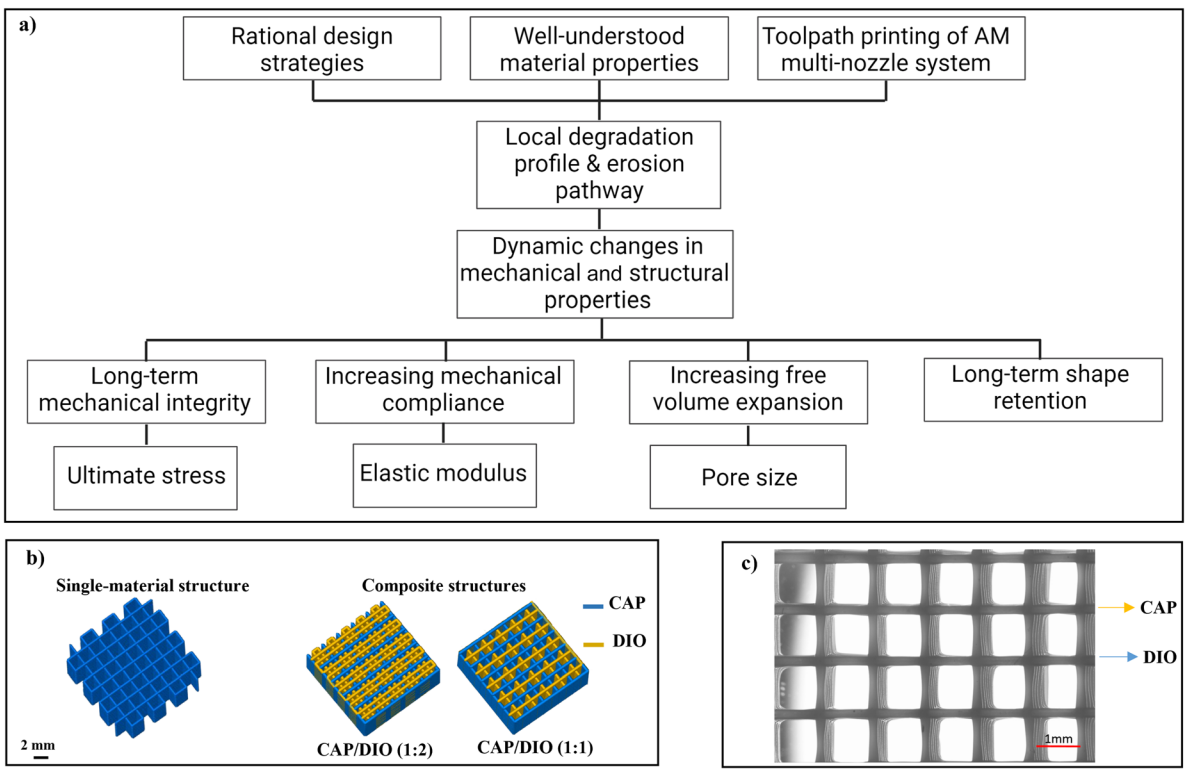

Fig. 1 (a) In this study, it is suggested that spatial placement of multiple materials in a composite fashion combined with well-understood material properties and rational design strategies allows for a tailored erosion pathway and controlled changes in mechanical and structural characteristics essential for SGSTR. (b) The composite structures with alternating CAP/DIO struts were developed *via* toolpath planning to tailor dynamic changes in mechanics and internal architecture. (c) The macroscopic images of 3D printed composite scaffolds with alternating CAP/DIO struts.

tures and dynamically modulate their architectural and mechanical changes over time. A multi-material scaffold was developed by integrating biodegradable polymers—specifically poly(glycolide-*co*-lactide) and polydioxanone—with advanced 3D printing technology. The aim was to precisely tune the scaffold's mechanical strength and degradation rate, ensuring that it meets the requirements for long-term soft tissue regeneration.

Materials and methods

Scaffold manufacturing

Caproprene™ 100 (CAP, 95% polycaprolactone, 5% poly(glycolide-*co*-lactide)) and Dioxaprene® 100 M (DIO, 100% polydioxanone) were supplied by Poly-Med, Inc. (Anderson, SC, USA) in the form of FDM filaments.

A 3D printer (FlashForge Dreamer, Jinhua, China) with two nozzles was used to print single-material and composite structures. As described previously,[4] the printing conditions for DIO and CAP were adjusted to a feed rate of 1800 mm min^{-1}, a nozzle temperature of 120 °C and a nozzle diameter of 0.2 mm. Single-material scaffolds of DIO and CAP were printed with a pore size of 1 ± 0.05 mm and dimensions of 10 × 10 × 5 mm^3. A design framework with alternating struts of CAP and DIO was established to print multi-material scaffolds. Using MATLAB programming and toolpath planning, nozzle movement corresponding to each material was controlled to deposit the material in pre-designed locations. By programming-assisted dual printing, composite scaffolds were fabricated with different ratios of CAP/DIO struts: 1 : 1 and 1 : 2, corresponding to pore sizes of 1 mm and 0.5 mm, respectively (Fig. 1).

Degradation

In vitro degradation of additively manufactured composite scaffolds is a worthwhile pursuit from a design point of view to understand the effects of material placement better. The degradation study was initially conducted on single-material scaffolds of CAP and DIO to determine which accelerated degradation conditions most closely mimic the degradation kinetics and mechanism observed under neutral conditions. Following these results, the composites of CAP/DIO were degraded under the appropriate accelerated conditions.

Single-material scaffolds

The erosion pathways of single-material scaffolds of DIO and CAP were evaluated in 1 M hydrochloric acid at pH 0 (HCl, Sigma-Aldrich, St. Louis, MO, USA), 5 M sodium hydroxide at pH 14 (NaOH, Sigma-Aldrich, St. Louis, MO, USA) and phosphate-buffered saline at pH 7 (PBS, Sigma-Aldrich, St. Louis, MO, USA) to determine which accelerating medium most closely approximates the degradation kinetics and mechanism observed under neutral conditions. Briefly, separate samples were immersed in 10 mL of each solution and incubated at 37 °C. At each timepoint, mass loss analysis, compression analysis, differential scanning calorimetry (DSC) and morphological analysis were conducted (n = 5) according to the following protocols.

Mass loss analysis. Samples were removed from the solution, washed three times with deionized water, and incubated under vacuum overnight before measuring mass loss.

Compression analysis. Samples were immersed in a water bath at 37 °C, and unconfined, uniaxial compression tests were performed up to 50% with a strain rate of 0.1 mm s^{-1} on an Instron Micro Tester (5848, Instron, Melbourne, Australia). The elastic modulus was calculated as the initial slope of the stress–strain curve, between 5 and 10% strains.

Thermal DSC analysis. Samples ranging from 3 to 5 mg were sealed in aluminium pans and exposed to non-isothermal heating at a ramp rate of 10 °C min^{-1} using a Q100 DSC (TA Instruments, Newcastle, DE, USA). Based on their known thermal properties, the temperature range used was 0 to 120 °C for DIO and 0 to 100 °C for CAP, with analysis performed on the thermographs using Universal Analysis 2000 software (TA Instruments, Newcastle, DE, USA). Since there was no available literature information regarding the melting enthalpy of the 100% crystalline CAP and DIO, it was not possible to calculate the crystallinity. Instead, the melting enthalpy of samples at different degradation timepoints was calculated, indicating relative crystallinity.

Morphological analysis. Samples were observed under a scanning electron microscope (SEM, JSM-7001F, JEOL Ltd, Tokyo, Japan). For cross-sectional views, samples were flash-frozen in liquid nitrogen (5 min) and cut with a scalpel blade. The samples were gold sputter-coated using a JEOL fine sputter coater (JFC-1200, JEOL Ltd, Tokyo, Japan) for 75 s at 8 mA current and observed under vacuum at 2 kV accelerating voltage.

Multi-material scaffolds

The degradation study on single-material scaffolds indicated that acidic conditions resulted in a degradation profile most similar to that observed under neutral conditions. Hence, accelerated degradation of multi-material scaffolds was conducted in 1 M HCl. Samples with dimensions of 10 × 10 × 5 mm^3 were immersed in 10 mL of the acidic solution and incubated at 37 °C. At 6 hours post-incubation, when DIO struts became highly fragile, the scaffold architecture, fibre morphology, compressive elastic modulus and failure strain were evaluated and compared with non-degraded controls (n = 5).

In vivo biodegradation and biocompatibility study

Surgery. The degradation pathway and dynamic changes of CAP/DIO (ratio of 1 : 1) composites were assessed in rats. Two groups of single-material scaffolds composed of DIO and CAP were also implanted as control groups. Six scaffolds, consisting of two from each group (DIO, CAP and CAP/DIO), were implanted subcutaneously into each rat (n = 5 per timepoint) for three and six months. According to the University of

Queensland animal housing standards, fifteen adult female or male Sprague Dawley rats were purchased from the Animal Resource Centre (Western Australia) and housed in a temperature-controlled, pathogen-free environment. All animal procedures were performed per the Guidelines for Care and Use of Laboratory Animals of the University of Queensland and approved by the Animal Ethics Committee of the University of Queensland (Ethics number: DENT/359/18).

The rat subcutaneous model was adapted from a previous study.[13] The skin of the dorsal area was shaved using an electric clipper or depilatory device, and then the skin was scrubbed with betadine antiseptic. Six full-thickness incisions through the skin (7 to 9 mm) were then created parallel to the dorsal midline. Blunt surgical scissors were used to delineate the skin from the underlying muscles fully. Once the subcutaneous socket was made, the 3D printed scaffolds 5 × 5 × 3 mm^3 were inserted. The skin incision was closed afterwards using surgical staples (size 9) to ensure healing. The rats were transferred into a clean, warm cage to facilitate full recovery. For two days post-surgery, Meloxicam (1 mg kg^{-1}) and Kefzol (20 mg kg^{-1}) were administered subcutaneously (in the ventral area) to provide analgesia and antimicrobial cover. An oral analgesic (Tramadol) was also used post-operatively to alleviate pain and discomfort. At each timepoint, the animals were euthanized using CO_2 at a fill rate of 10 to 30% of the chamber volume per minute. The scaffolds were then surgically removed.

Compression analysis. Five scaffold samples were immersed in a PBS bath at 37 °C and analysed under mechanical compression at a rate of 0.1 mm s^{-1}.

Non-isothermal DSC analysis. The same samples were then used for DSC analysis. CAP and DIO fibres were removed from the scaffolds and analysed under non-isothermal conditions at a heating rate of 10 °C min^{-1}. In addition, at each timepoint, five samples were fixed in 4% paraformaldehyde (PFA) for 24 hours before being transferred into 70% ethanol for macroscopic inspection, SEM, micro-computed tomography (μCT), histology and immunohistochemistry.

Micro-computed tomography (μCT)

At three and six months post-implantation, the samples were scanned and analysed *via* μCT (μCT 50, Scanco Medical, Brüttisellen, Switzerland). All samples were scanned in 70% ethanol at 45 kV and 200 μA, with an isotropic voxel size of 5 × 5 × 5 μm^3 and a sample time of 1.32 s. Due to the low density of the samples and the long sample time, ring artefacts became apparent in the greyscale images. These artefacts could be partially reduced by postprocessing the raw scan data. 3D reconstruction of the final grey-scale image stack for qualitative analysis was performed using Drishti,[14] an open-source scientific visualization software. A region of interest (ROI) containing the polymer scaffold was selected for two purposes: firstly, to reduce background noise and secondly, to significantly reduce the dataset size from 8 to 3 GB. A transfer function was chosen to make the scaffold fibres visible within the tissue. The colour intensity was normalized across all three datasets and corresponded to the amount of polymer remaining within the tissue for each timepoint.

Histology and immunohistochemistry

After μCT evaluation, one sample from each group and timepoint was paraffin processed using a tissue processor (Excelsior ES tissue processor) overnight and embedded in molten paraffin at 60 °C, using the Shandon Histocentre 3 embedding station (Thermo Scientific). Using a Leica RM2235 rotary microtome (Leica Biosystems; Nussloch, Germany), paraffin sections were cut at 5 μm, flattened in a water bath (Labec, Marrickville, Australia) at 42 °C and collected onto Polysine™-coated microscope slides (Thermo Scientific). The paraffin slides were dried for 16 h at 60 °C prior to histological and immunohistochemical staining. Using a Leica Autostainer XL (Leica Biosystems), two slides (slide 1 and slide 10) were stained with eosin and haematoxylin (H&E) to evaluate the morphological and structural compliance of the implanted scaffolds.

For immunohistochemistry evaluation, five tissue sections (n = 5) were used for each antibody. The following antibodies were used: anti-alpha smooth muscle actin (α-SMA, 1 : 500, abcam, ab7817, RRID: AB_262054) to evaluate the newly formed fibrous tissue, cluster of differentiation 68 (CD68, 1 : 500, abcam, ab125212, RRID: AB_10975465) to evaluate overall macrophagic activity, inducible nitric oxide synthase (iNOS, 1 : 1000, abcam, ab15323, RRID: AB_301857) to assess pro-inflammatory macrophage (M1) activity and cluster of differentiation 163 (CD163, 1 : 100, abcam, ab182422, RRID: AB_2753196) to evaluate pro-regenerative macrophage (M2) activity.

Briefly, slides were first dewaxed in 2 changes of xylene for 3 min each and then transferred to 100% ethanol for 2 min, followed by decreasing ethanol changes of 90, 80, 70 and 50% for 1 min each. The slides were then incubated in DAKO wash buffer (1 : 10, Dako, cat. no. DM831) for 1 min. Each paraffin slide was then delineated using a DAKO pen (Dako, cat. no. S2002). Enzyme-mediated antigen retrieval was not performed due to high amounts of unspecific antibody binding observed during antibody optimization. Endogenous peroxidase activity was blocked with 3% (vol/vol) hydrogen peroxidase (30%; Sigma-Aldrich, cat. no. H3410) for 5 min, followed by washing in 3 changes of Dako wash buffer. Nonspecific binding sites were blocked with 2% (wt/vol) bovine serum (BSA, Sigma-Aldrich, cat. no. A7906) for α-SMA and CD163 for 30 min and 60 min using CD68. The iNOS nonspecific background was blocked with a background sniper (Biocare Medical LLC, Background sniper, cat. no. BS966) for 10 min. Before primary antibody incubations, α-SMA, CD163 and CD68 primary antibodies were diluted in BSA, and iNOS was diluted in a Dako antibody diluent (Dako Antibody Diluent with Background Reducing Components, cat no. S3022). Samples were then incubated with primary antibodies for 1 h at room temperature. The slides were individually washed in 3 changes of Dako wash buffer and subsequently incubated in a secondary antibody (Dako, EnVision+ dual-link system (HRP rabbit/mouse

kit)). 2% BSA was used as an isotype for α-SMA, CD68 and CD163, and a normal rabbit serum control (Rb Primary Antibody Isotype Control, Life Technologies, cat. no. 08-6199) was used as an isotype for iNOS. The slides were then washed in 3 changes of Dako washer buffer and immunoreactivity was detected *via* color development with a liquid diaminobenzidine (DAB) chromogen (Dako/Agilent, cat. no. K3468), according to the specific primary antibody (α-SMA: 40 s; CD68: 25 s; CD163: 52 s; and iNOS: 80 s). Following colour development, the samples were washed in 1 change of Dako wash buffer, counterstained and coverslipped using a Leica Autostainer XL. Further reagent set-up instructions can be found in Sparks *et al.*[15] Stained paraffin slides were scanned in full using a 3DHistech Scan II Brightfield slide scanner (3DHistech, Budapest, Hungary) with a 20X objective. Using the CaseViewer 2.2 platform, images were exported and assembled according to each scaffold and timepoint of scaffold implantation.

Statistical analysis

Quantitative assessment of α-SMA, CD68, iNOS and CD163 was performed using a MATLAB algorithm according to Medeiros Savi *et al.*[16] Statistical analysis was conducted using GraphPad Prism version 7.03. The means of the different treatment groups were compared within the same animal (and thus within the same timepoint), focusing on the treatment group as a fixed effect. Given that 4 out of 36 datasets were not normally distributed (as determined by the Shapiro–Wilk test), the dataset was analysed using nonparametric tests (Kruskal–Wallis and Mann–Whitney tests). Five tissue sections ($n = 5$) were used for each antibody.

Results

In vitro erosion pathway of single-material scaffolds under basic, neutral and acidic conditions

Degradation mechanisms and kinetics for DIO. Degradation of DIO under acidic and neutral conditions was assessed for 6 hours and 54 days, respectively. As shown in Fig. 2(a), both conditions induced similar morphological changes with a three-step attack: (1) slight surface erosion of amorphous regions with visible grain boundaries on the surface of struts; (2) degradation of interlamellar regions, leading to the formation of small cracks; and (3) propagation of large longitudinal and circumferential cracks, leading to loss of mechanical stability and structural support. Over 4 hours of degradation under acidic conditions, the elastic modulus decreased by >90% (from 7.82 MPa to 0.1 MPa), corresponding to a mass loss of 2.2%, followed by total disintegration and a mass loss of 5.9% after 6 hours of degradation (Fig. 2(b) and (c)). A similar trend was observed under neutral conditions where slight fibre thinning and a mass loss of 4.3% were observed before disintegration (Fig. 2(a) and (b)). At 40 days post-incubation, a >90% reduction in elastic modulus was observed (from 7.82 MPa to 0.38 MPa), corresponding to similar changes for a 4 hour incubation period in acidic medium. DSC analysis showed a continuous increase in crystallinity under both conditions, with a >37% increase in melting enthalpy from 66.0 to 120.1 J g^{-1} under acidic and 95.9 J g^{-1} under neutral conditions (Fig. 2(d)). These observations indicate that bulk degradation is the predominant erosion pathway, in which the rate of water diffusion into the scaffold matrix is faster than polymer chain scission. This mechanism is well documented for several aliphatic polyesters. It involves diffusion of the by-products of hydrolysis from the core of the strut to the surrounding medium at a comparatively slow rate, resulting in only a minor reduction in mass and fibre thickness. This process produces small cracks on the strut surface, which are enlarged as degradation proceeds until near-complete disintegration of the whole structure occurs. Hydrolysis of the amorphous regions and recrystallization of shortened polymer chains within the scaffold matrix increased overall crystallinity, which is corroborated by the DSC analysis.

Base-catalysed degradation of DIO was evaluated for up to 160 minutes. Hydrolytic attack was noticeable on the surface and exhibited a two-step degradation process (Fig. 2(a)). Minor pitting initially appeared on the surface and was followed by larger cavities on the roughened surface until near-complete disintegration. As degradation proceeded, a gradual reduction in fibre thickness, mass and elastic modulus was observed. A mass loss of 30.8% was noted, with the elastic modulus reduced by 37.4% (from 7.82 MPa to 2.9 MPa) (Fig. 2(b) and (c)). DSC analysis indicated a continuous increase in melting enthalpy from 66.0 to 72.0 J g^{-1}, indicative of increasing crystallinity (Fig. 2(d)). Taken collectively, these data confirm that degradation predominantly occurred *via* surface erosion, where the water penetration and diffusion rate is slower than polymer scission and hydrolysis. In this mechanism, cavities appear on the surface, hydrolytic by-products easily diffuse into the surrounding medium and mass loss and fibre thinning are observed.

From a mechanical standpoint, the reduced contact area at fusion points caused by significant fibre thinning and mass loss is the underlying reason for strength reduction and mechanical failure. However, under acidic and neutral conditions, cracks resulting from bulk degradation of the construct are the primary mode of failure.

Degradation mechanism and kinetics for CAP. Degradation of CAP was examined for seven weeks under acidic and 15 months under neutral conditions. Under both conditions, CAP scaffolds exhibited a wavy pattern on the surface with minor changes in fibre thickness and mass loss (Fig. 3(a)). The wavy patterns can be associated with nematic domains of molten semi-crystalline polymers, which are ordered due to elongation and shear forces applied by the nozzle during the melt extrusion process.[17] The fast cooling rate of superficial surfaces leads to solidification of the aligned structures.[17] These domains, resistant to hydrolytic degradation, become visible after slight surface erosion and degradation of superficial amorphous regions. Under acidic conditions, minor fibre thinning and mass loss were observed (Fig. 3(b) and (c)). At the end of the seven week degradation study under acidic conditions, 5.1% mass loss was observed, the elastic modulus had increased from 4.7 to 16.5 MPa, and the ultimate strain had decreased

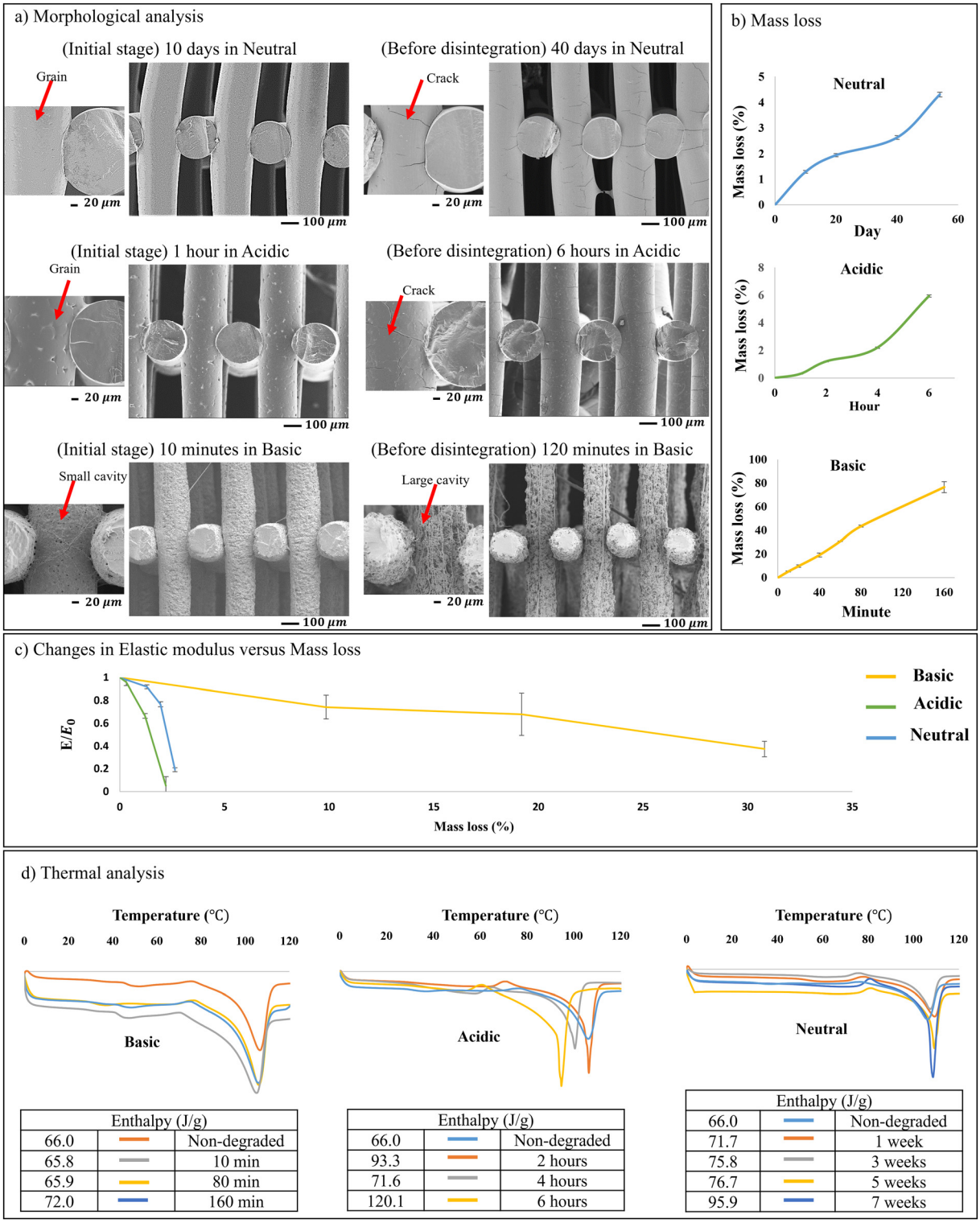

Enthalpy (J/g)		
66.0		Non-degraded
65.8		10 min
65.9		80 min
72.0		160 min

Enthalpy (J/g)		
66.0		Non-degraded
93.3		2 hours
71.6		4 hours
120.1		6 hours

Enthalpy (J/g)		
66.0		Non-degraded
71.7		1 week
75.8		3 weeks
76.7		5 weeks
95.9		7 weeks

Fig. 2 *In vitro* degradation of DIO under basic, acidic and neutral conditions. (a) Morphological study conducted *via* SEM analysis (n = 3). (b) Mass loss calculated at each timepoint over the degradation period (n = 5). (c) Ratio of elastic modulus (E) to initial elastic modulus (E_0) plotted *versus* mass loss to correlate changes in mass and mechanical properties (n = 5). (d) Thermal DSC analysis for degraded and non-degraded samples to evaluate changes in the polymer crystallinity (n = 3).

from 22.2 to 0.1%. These data illustrate the embrittlement of CAP when exposed to acidic pH and can be correlated with an increase in crystallinity (demonstrated by increasing melting enthalpy from 70.2 to 102.0 J g^{-1}) (Fig. 3(d)). Under neutral conditions, after 15 months, a 1.5% mass loss was noted while the elastic modulus initially decreased from 4.7 to 2.6 MPa and

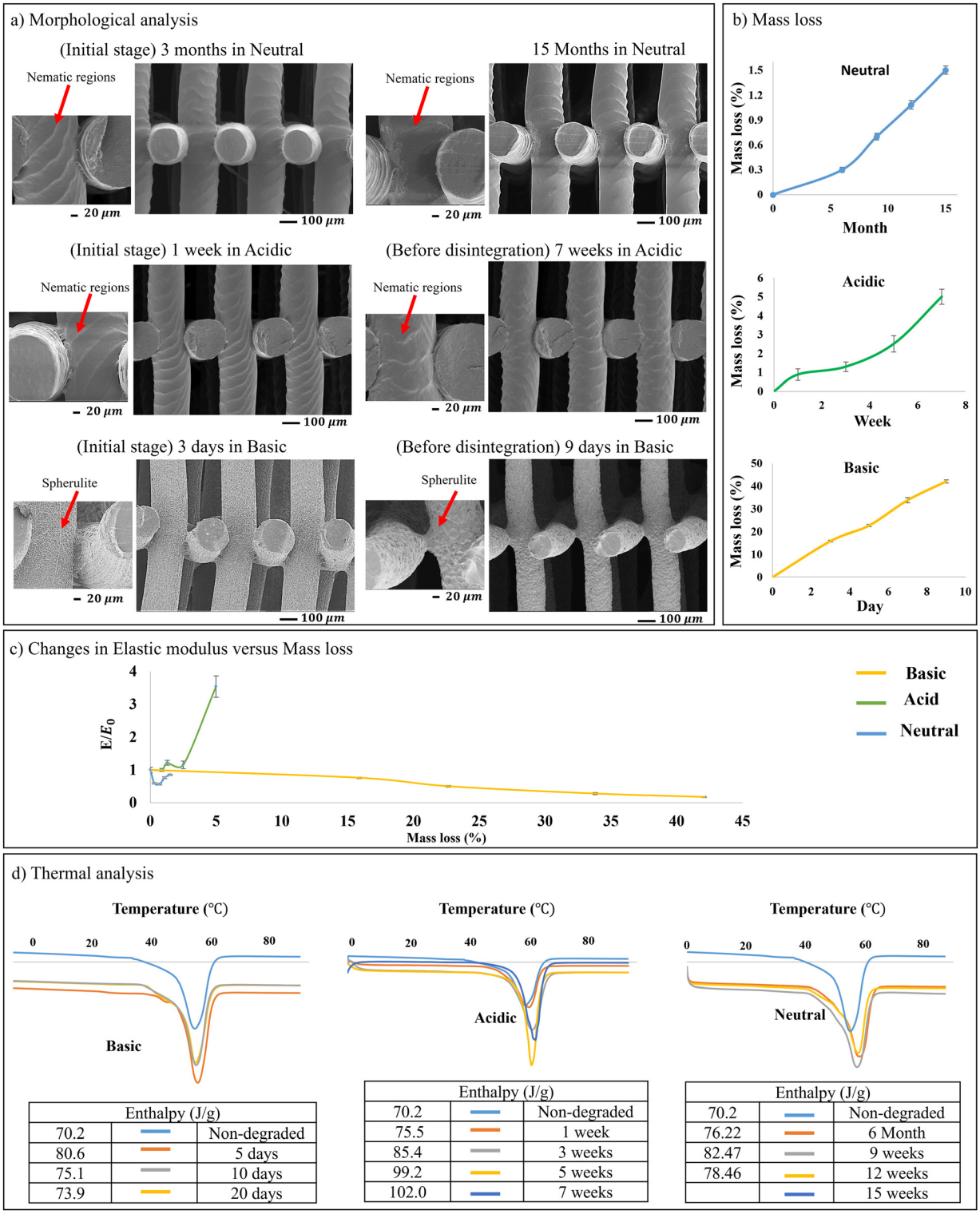

Fig. 3 *In vitro* degradation of CAP under basic, acidic and neutral conditions. (a) Morphological study conducted *via* SEM analysis (n = 3). (b) Mass loss calculated at each timepoint over the degradation period (n = 5). (c) Ratio of elastic modulus (E) to initial elastic modulus (E_0) plotted *versus* mass loss to correlate changes in mass and mechanical properties (n = 5). (d) Thermal DSC analysis for degraded and non-degraded samples to evaluate changes in the polymer crystallinity (n = 3).

then increased to 3.9 MPa (Fig. 3(b) and (c)). These data imply that bulk erosion is the predominant degradation pathway of CAP under neutral and acidic conditions, where slow diffusion of hydrolysis by-products results in only slight mass loss and fibre thinning, while the change in mechanical properties is due to changes in crystallinity.

Hydrolytic attack in a basic environment is notably more aggressive compared to acidic and neutral conditions, producing large cavities on the surface along with significant mass loss and fibre thinning (Fig. 3(a)). Due to severe surface erosion and greater access of water to the interior amorphous regions, spherulite regions are noticeable and prominent on the strut surface with a decrease in elastic modulus of more than 80% (from 4.7 MPa to 0.85 MPa) at 42.1% mass loss after 9 days (Fig. 3(c)). From a mechanical standpoint, the decrease in fibre thickness and subsequently the contact area at the fusion points due to the surface erosion pathway is the primary cause of mechanical loss. DSC analysis revealed an initial increase in crystallinity, evidenced by the rise in melting enthalpy from 70.2 to 80.6 J g^{-1}, followed by a decrease to 73.9 J g^{-1} (Fig. 3(d)).

In vitro erosion pathway of CAP/DIO composites under acidic conditions

Composites with alternating struts of CAP and DIO were developed to address long-term integrity while modulating an expansion of the scaffold pore size and an increase in the mechanical compliance of the scaffold during degradation. To assess these dynamic changes, composites were degraded in 1 M HCl to simulate, in an accelerated manner (acidic conditions), the degradation pathway of DIO and CAP under neutral conditions. Over a 6 hour incubation period, morphological analysis showed bulk degradation of DIO fibres and the formation of severe cracks similar to those observed under neutral conditions (Fig. 4(a)). DIO fibres became highly fragile, whereas CAP fibres remained intact and preserved the integrity of the overall structure. Extreme care was taken to handle the composite for SEM and avoid disintegration of DIO fibres. The composites with a CAP/DIO ratio of 1 : 1 exhibited a 2.2-fold reduction in elastic modulus from 5.84 to 2.67 MPa and an increase in pore size from 0.5 to 1 mm after 6 hours (Fig. 4(b) and (c)). By increasing the CAP/DIO ratio to 1 : 2, a 3.2-fold decrease in elastic modulus from 8.51 to 2.67 MPa was noted, with an increase in pore size from 1 to 2 mm.

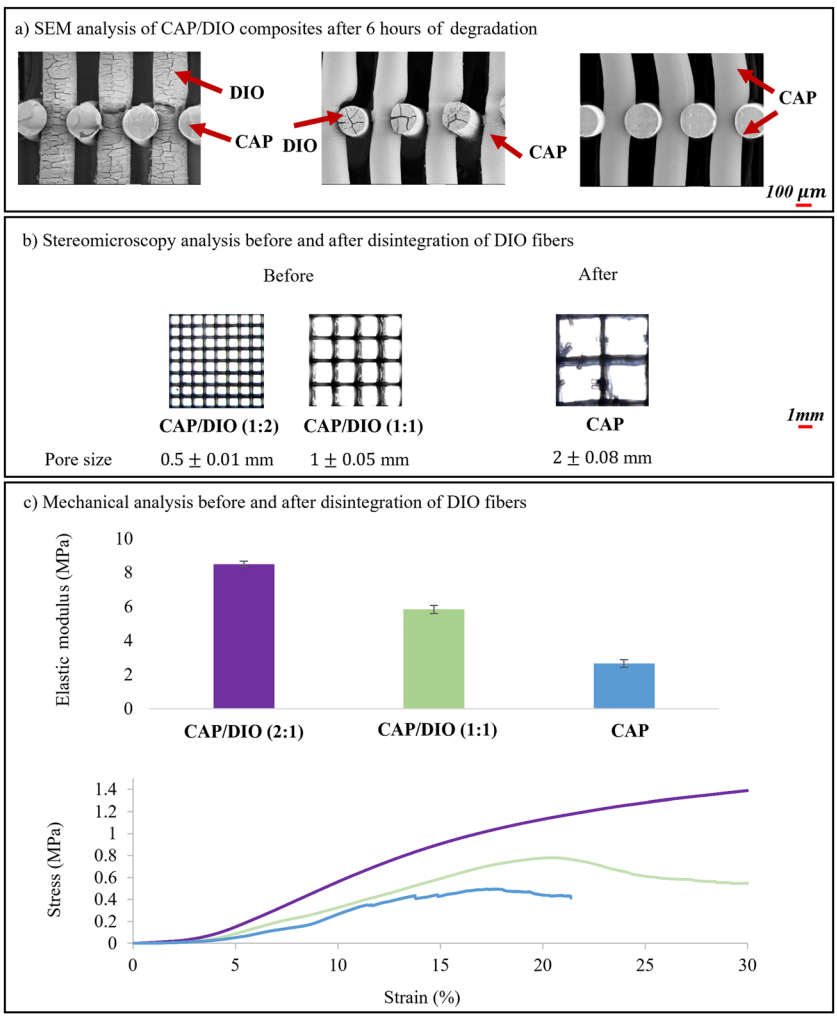

Fig. 4 *In vitro* degradation of DIO/CAP under acidic conditions. (a) Morphological study conducted *via* SEM analysis (n = 3). (b) Stereomicroscopy images of the composites before and after degradation to calculate the pore size (n = 5). (c) Changes in mechanical response and elastic modulus of the composites under compression (n = 5).

In vivo erosion pathway of CAP/DIO composites *versus* single-material scaffolds of CAP and DIO

CAP/DIO composites and single-material scaffolds of CAP and DIO were implanted in rats for six months to investigate and compare their degradation pathway and subsequent structural changes.

In vivo erosion pathway of single-material scaffolds of DIO and CAP

DIO scaffolds exhibited a rapid degradation rate and decreased elastic modulus and structural integrity (Fig. 5(a)). Within the first month, the elastic modulus of DIO decreased from 7.82 to 2.06 MPa, followed by a rapid reduction to 0.03 MPa over three months and full degradation over six months (Fig. 5(a)). DSC analysis showed a 7% increase in melting enthalpy at the first timepoint (Fig. 5(b)); however, due to severe DIO disintegration at three and six months, we were not able to extract DIO fibres from the surrounding tissue to complete the DSC analysis. Compared to the *in vitro* degradation results, *in vivo* degradation of DIO exhibited a bulk erosion pathway with a decrease in elastic modulus and an increase in melting enthalpy, similar to what was observed under neutral and acidic conditions.

In contrast to DIO, the CAP scaffold remained robust mechanically with slight bulk erosion and higher melting enthalpy (21.8%), which resulted in changes in elastic modulus from 5.58 to 5.97, 6.39 and 6.92 MPa after one, three and six months post-implantation, respectively. The increased elastic modulus and melting enthalpy of CAP after six months of implantation are in agreement with *in vitro* accelerated degradation of CAP under acidic and neutral conditions.

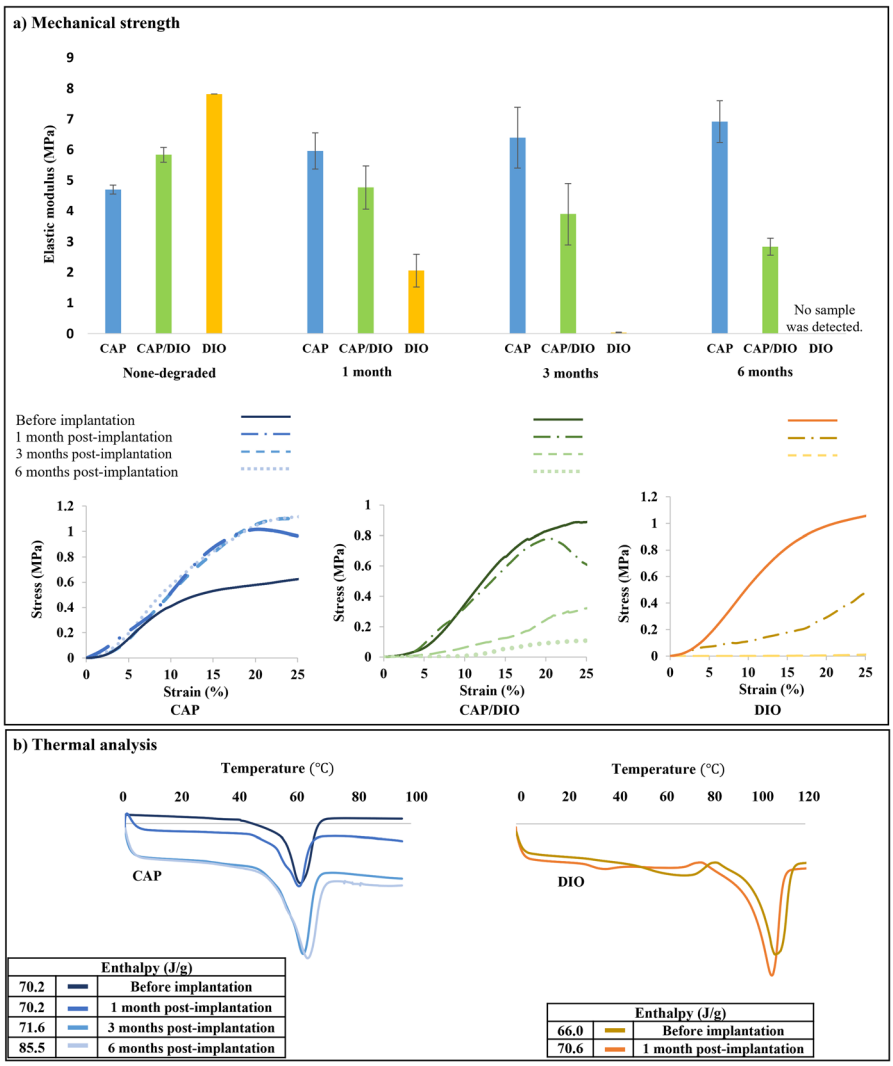

Fig. 5 Scaffold properties after *in vivo* degradation of CAP/DIO composites *versus* single-material scaffolds of CAP and DIO. (a) Within six months of implantation, the elastic modulus of CAP/DIO composites gradually decreased, while DIO exhibited a faster reduction and disintegration until complete absorption (no sample could be detected for DIO groups after six months of implantation). In contrast, CAP exhibited an increasing rate in elastic modulus and embrittlement (n = 5). (b) Non-isothermal DSC analysis illustrated an increase in the crystallinity of CAP and DIO struts during *in vivo* degradation (n = 3).

In vivo erosion pathway of CAP/DIO composites

CAP/DIO composites followed a significantly different degradation pathway compared to single-material scaffolds of CAP or DIO. The overall integrity of the composite was preserved, while the elastic modulus decreased from 5.84 to 4.77, 3.91 and 2.84 MPa at one, three and six months post-implantation, respectively (Fig. 5(a)). Morphological analysis revealed that over three months, DIO struts were cracked and broken without major fibre thinning, followed by complete absorption after the entire six-month period (Fig. 6(a) and (b)), which led to a controlled increase in pore size from 1 to 2 mm and a higher compliance in mechanical response. CAP fibres remained stable and well connected at the fusion points and retained the integrity of the composite structure (Fig. 6(a) and (b)). Therefore, over the six-month implantation period, the composite exhibited long-term structural retention with increased scaffold compliance (a decrease in compressive elastic modulus) and a 50% increase in pore size.

Tissue response to the erosion pathway observed in single-material and composite scaffolds

DIO scaffold. Partial degradation of DIO was observed within the first month, followed by total disintegration after three months (Fig. 7(a1) and (a2)). Initially, DIO struts guided tissue formation and were partially replaced by a provisional tissue matrix (Fig. 7(a1) and (a2) and Fig. S1(a1) and a(2),† black arrows), where a few foreign giant cells could be observed (Fig. 7(a3)). However, after total disintegration in three months, the newly formed tissue was not supported mechanically by the scaffold and could not retain its overall shape (Fig. 7(a4) and Fig. S1 (a4)†). The remnants of DIO struts left in the disorganised newly formed tissue were also surrounded by foreign body giant cells (Fig. 7(a5) and (a6), black arrows), possibly increasing the excretion of the rapidly degrading DIO material.

α-SMA expression. Within three months, no signs of fibrotic reaction were detected through the α-SMA (Fig. 7(b1) and (b2)) antibody marker. However, the provisional tissue formed around the remnants of DIO struts was highly vascularized

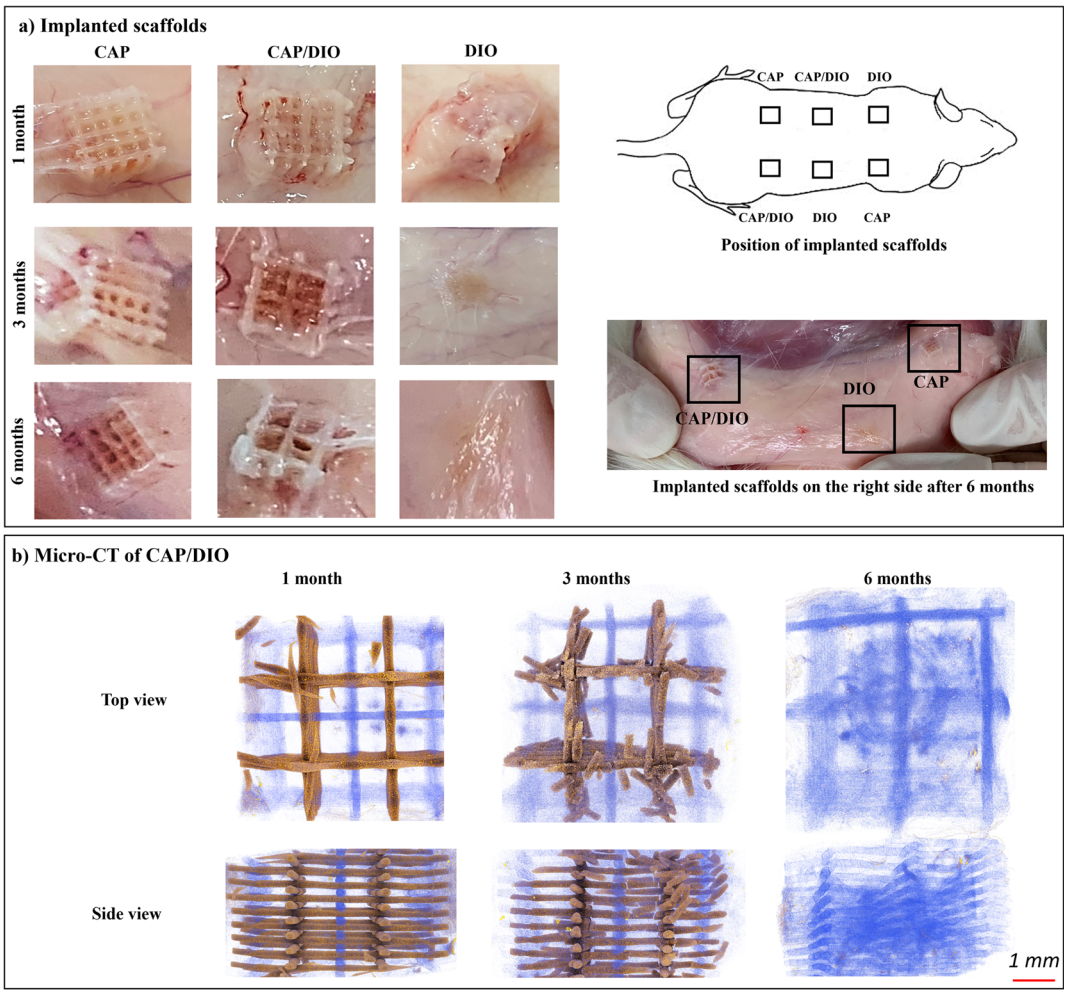

Fig. 6 (a) Implanted scaffolds within six months of implantation in rats (n = 5). (b) μCT analysis of CAP/DIO composites (n = 2).

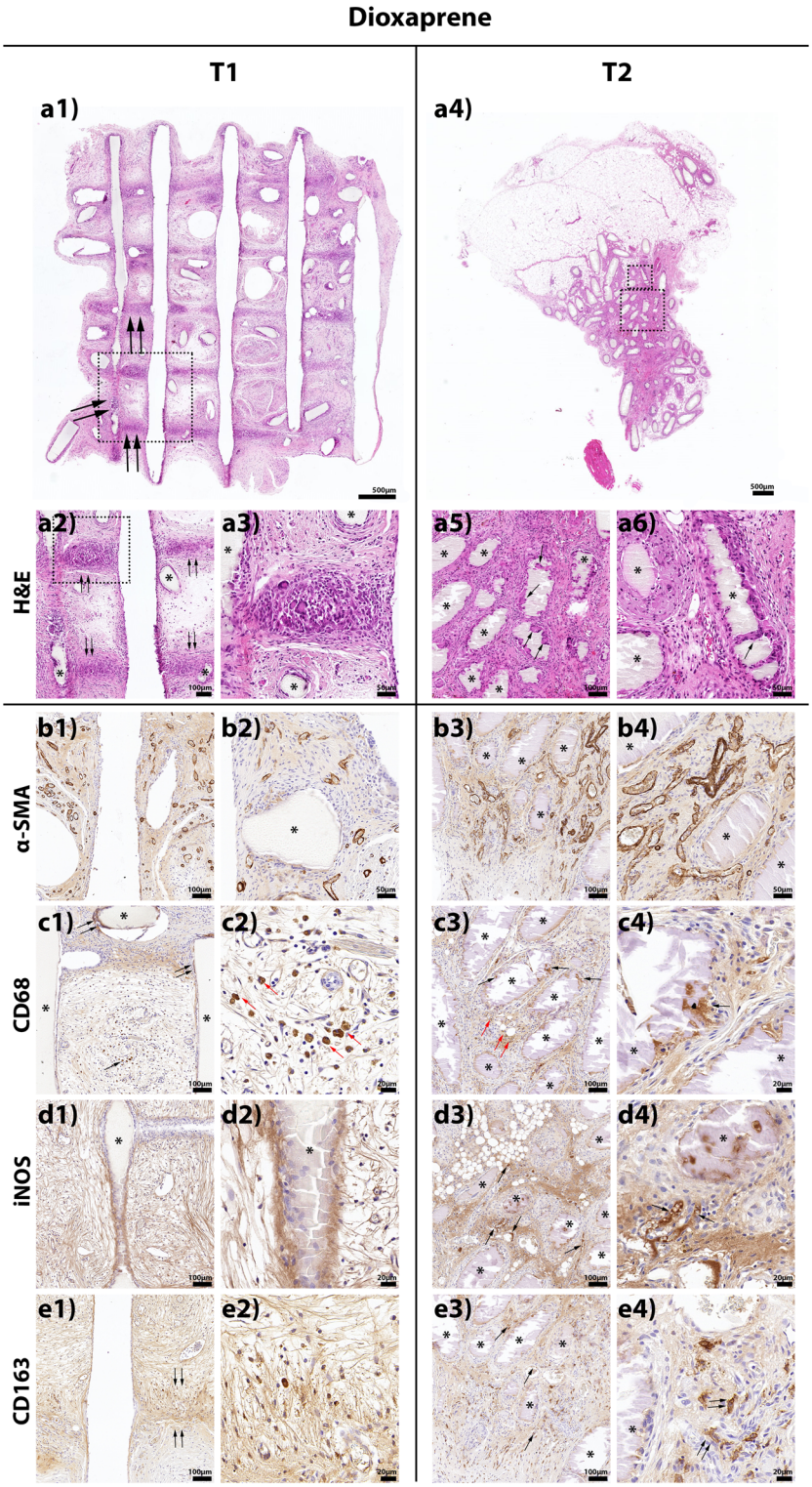

Fig. 7 H&E and immunohistochemical analysis of the DIO scaffolds at the one (T1) and three (T2)-month timepoints (n = 5). H&E images show partial degradation of DIO at one month (a1–a3) and complete disintegration after 3 months (a4–a6). Initially, DIO struts guided tissue formation, while being replaced by a provisional matrix (a1 and a2, double arrows). By three months, the tissue lost integrity (a4), and the DIO remnants were surrounded by foreign body giant cells (a5 and a6, single arrows). α-SMA staining (b1–b4) revealed no fibrotic reaction, though the tissue around DIO remnants was highly vascularized. CD68 expression (c1–c4), indicating macrophage activity, was observed at the edges of fragmented DIO (c1, black double arros and c3 and c4, black arrows) and near blood vessels (c1, black arrow and c2, c3, red arrows). iNOS, a pro-inflammatory marker (d1–d4), showed strong expression around the DIO strut edges (d1 and d2), especially in lymphatic vessels at three months (d3 and d4, black arrows). CD163, marking tissue-repair macrophages (e1–e4), was seen within the tissue matrix at one month (e1, double arrows and e2) and near blood vessels (e3, black arrows) and fibroblasts at three months (e4, double black arrows). Asterisks indicate DIO remnants.

(Fig. 7(b1) and (b2)). Although loose collagen fibres could be observed at the edges of struts, no signs of fibrotic encapsulation were observed (ESI Fig. S1(b1) and (b3),† respectively).

CD68, iNOS, and CD163 expression. Positive expression of CD68 (Fig. 7(c1–c4)), a macrophage marker for pro-inflammatory (M1) and anti-inflammatory (M2) types, was mainly observed at the outer edges of the fragmented DIO (Fig. 7(c1), (c3) and (c4), black arrows, and ESI Fig. S1(c1) and (c4)†) and within the newly formed tissue, where macrophage footprints could be seen around blood vessels (Fig. 7(c2) and (c3), red arrows). High expression of iNOS, a pro-inflammatory M1 macrophage marker, was observed at the outer edges and surface of the DIO struts for both timepoints (Fig. 7(d1–d3) and Fig. S1 (d1–d4)†), especially within lymphatic vessels at three months (Fig. 7(d3) and (d4), black arrows). CD163 expression, an M2 macrophage marker involved in tissue repair, was mainly observed both within the newly formed tissue (Fig. 7(e1) and (e2), black arrows, and ESI Fig. S1(e1) and (e2)†) at the one-month timepoint and in the vicinity of blood vessels (Fig. 7(e3), black arrows) and fibroblast cells after three months (Fig. 7(e4), double black arrows).

CAP scaffold. CAP struts retained their structural integrity throughout the six months of the experiment (Fig. 8(a1–a3) and Fig. S2(a1–a6)†). The formation of a provisional matrix composed mainly of adipose tissue in the centre of the pores (Fig. 8 (a4) and (a5), red arrows) with a few sparse fibres arranged at the strut fusion points was observed at the one-month timepoint (Fig. 8(a4) and (a5), black arrows). At the three-month timepoint, giant cells could be observed at strut fusion points (Fig. 8(a6), black arrows) as well as an increased number of cells lining the outer surface of the struts (Fig. 8(a7), black arrows). At six months, the cells still appeared to be packing around the scaffold fusion points (Fig. 8(a8) and (a9), double black arrows), and the fatty tissue formed within the scaffold pore spaces seemed to have been replaced by thicker collagen fibres packing around the fusion points (Fig. 8(a8) and (a9), red arrows).

α-SMA expression. This regular arrangement of collagen fibres at the outer edges of the struts and fusion points, especially at the one-month timepoint, was depicted by α-SMA positive expression (Fig. 8(b1) and ESI Fig. S2(b1–b4),† black arrows). However, no signs of fibrotic encapsulation were observed at any timepoint (Fig. 8(b1–b6) and Fig. S2(b1), (b3) and (b5)†). Instead, α-SMA expression indicated the presence of smooth muscle cells at the endothelial membrane of longitudinal and transverse capillaries and blood vessels within the provisional tissue formed (Fig. 8(b2–b6)).

CD68 expression. At the one-month timepoint, strong expression of CD68 was observed at the outer edges of the CAP struts (Fig. 8(c1), black arrows), especially at the fusion points where giant cells could be observed (Fig. 8(c2) and Fig. S2(c2),† black arrows). After three months, this response was extended to the newly formed provisional fibrous tissue (Fig. 8(c3) and ESI Fig. S2(c3 and c4)†) where monocyte cells were heavily stained within the adipose tissue and aggregates of the fibrin strands around the CAP surface (Fig. 8(c4), black arrows). After six months, the CD68 immunological reactivity observed within the newly formed fibrous tissue decreased (ESI Fig. S2(c5) and (c6)†) and was mainly localized at fusion points and within the cells lining the outer surface of the struts (Fig. 8(c5) and (c6), arrows).

Strong iNOS immunological activity was observed within the fibrous tissue formed around the 3D construct at all timepoints (Fig. 8(d1–d6)). However, the immunological pro-inflammatory activity, detected by iNOS at CAP fusion points and within the fibrous tissue, progressively decreased with time (Fig. 8(d1–d6) and Fig. S2(d1-d6)†).

CD163 expression. CD163 expression was initially located within the tissue surrounding the struts (ESI Fig. S2(e1)†), especially at the outer surface (Fig. 8(e1), black arrows, and ESI Fig. S2(e2),† black arrows) and at fibroblast cells (Fig. 8(e2), red arrows). At three months, CD163 was observed within aggregates of the fibrin strands around the CAP surface and at monocytes within the subcutaneous adipose tissue formed in the scaffold pore spaces (Fig. 8(e3) and (e4) and ESI Fig. S2(e3) and (e4)†). This response increased after six months, especially within blood vessels (Fig. 8(e5), black arrows, and ESI Fig. S2 (e6),† black arrows) and at fibroblasts within the newly formed fibrous tissue (Fig. 8(e6), red arrows).

CAP/DIO composites. Within six months of implantation, DIO struts were completely degraded and replaced with provisional tissue, whereas CAP struts retained the integrity of the scaffold structure and the newly formed tissue (Fig. 9(a1–a3) and Fig. S3(a1), (a3) and (a5)†).

At one- and three-month timepoints, the provisional matrix was mainly composed of adipose tissue within the centre of pores (Fig. 9(a4) and (a6), red arrows) and of loose fibrous tissue closely arranged around the CAP/DIO struts (Fig. 9(a4), (a8) and (a9) and Fig. S3(a2),† double black arrows). A few giant cells were also observed at the strut fusion points and surface (Fig. 9(a4), (a8) and (a9), single black arrows). At the six-month timepoint, DIO struts were fully degraded and replaced by a highly organized provisional epithelial tissue (Fig. 9(a3), (a8), (a9) and Fig. S3(a5) and (a6)†). This newly formed tissue, which was situated in the middle of enlarged pores (Fig. 9(a8) and Fig. S3(a5),† dotted line), was mechanically supported by CAP fibres and can be considered a substantial source of cells and blood vessels for further stages of tissue regeneration and angiogenesis within the pores.

α-SMA expression. At the one-month timepoint, slight immunological reactivity of α-SMA was observed at the loose fibrous tissue closely packed at the outer surface of the struts (Fig. 9(b1), red arrows) and at the endothelial walls of the newly proliferating longitudinal and transverse capillaries (Fig. 9(b2) and Fig. S3(b2)†). At three months, α-SMA expression was also observed within the sprouting capillaries around the degrading DIO struts (Fig. 9(b3), (b4), and Fig. S3(b4)†). However, this reactivity decreased by the six-month timepoint (Fig. 9(b5), (b6) and Fig S3(b6)†). No signs of fibrous encapsulation were observed at any timepoint (Fig. S3(b1), b(3) and (b5)†).

CD68 expression. At the one-month timepoint, CD68 expression was mainly observed at the endothelial wall membrane of blood vessels (Fig. 9(c1), (c2) and Fig. S3(c2),† black arrows). At three months, CD68 expression was seen at the con-

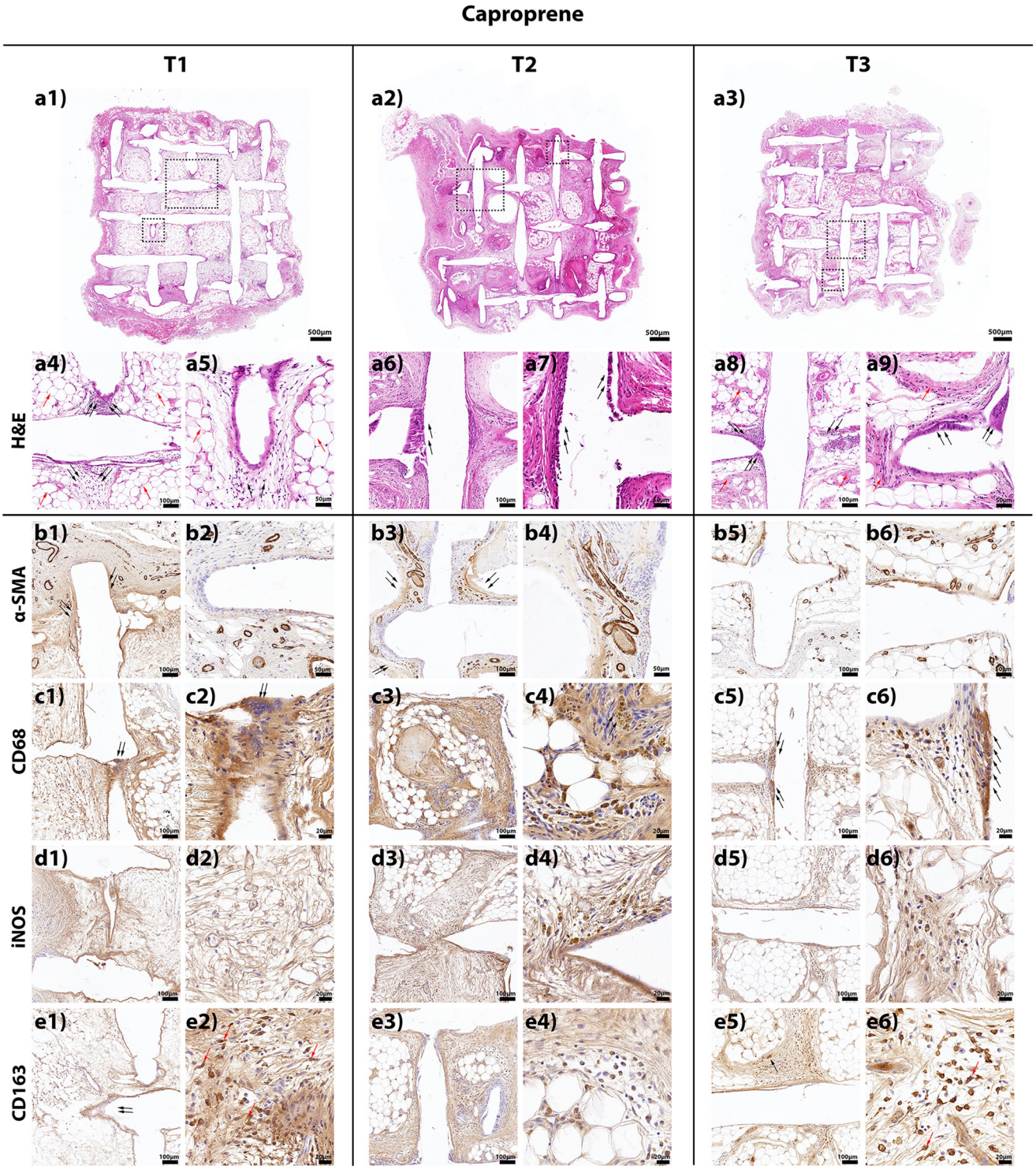

Fig. 8 H&E and immunohistochemical analysis of the CAP scaffolds at one (T1), three (T2) and six (T3)-month timepoints (n = 5). CAP struts maintained integrity throughout the six-month period (a1–a3). At one month, a provisional adipose matrix formed within the scaffold pores (a4 and a5, red arrows), with sparse fibers at fusion points (a4 and a5, black arrows). By three months, giant cells were observed at fusion points, with increased cell density lining the struts (a6 and a7, black arrows). At six months, cell agglomerating around fusion points (a8, double black arrows) and giant cells around the scaffold struts (a9, double black arrows) were observed. α-SMA staining showed smooth muscle cells around struts (b1 and b3, black arrows) and along capillary membranes at all timepoints (b1–b6). CD68 was strongly expressed at strut edges and fusion points with giant cells at one month (c1 and c2, black arrows), extending to fibrous tissue by three months (c3 and c4). At six months, the CD68 reactivity decreased and was localized to fusion points (c5 and c6, black arrows). iNOS was strongly expressed within the fibrous tissue throughout, with intensity decreasing over time (d1–d6). CD163 was seen at one and three months around struts (e1, black arrows) and within connective tissue (e2 red arrows, e3 and e4), increasing at six months in blood vessels (e5, black arrows) and fibroblasts (e6, red arrows).

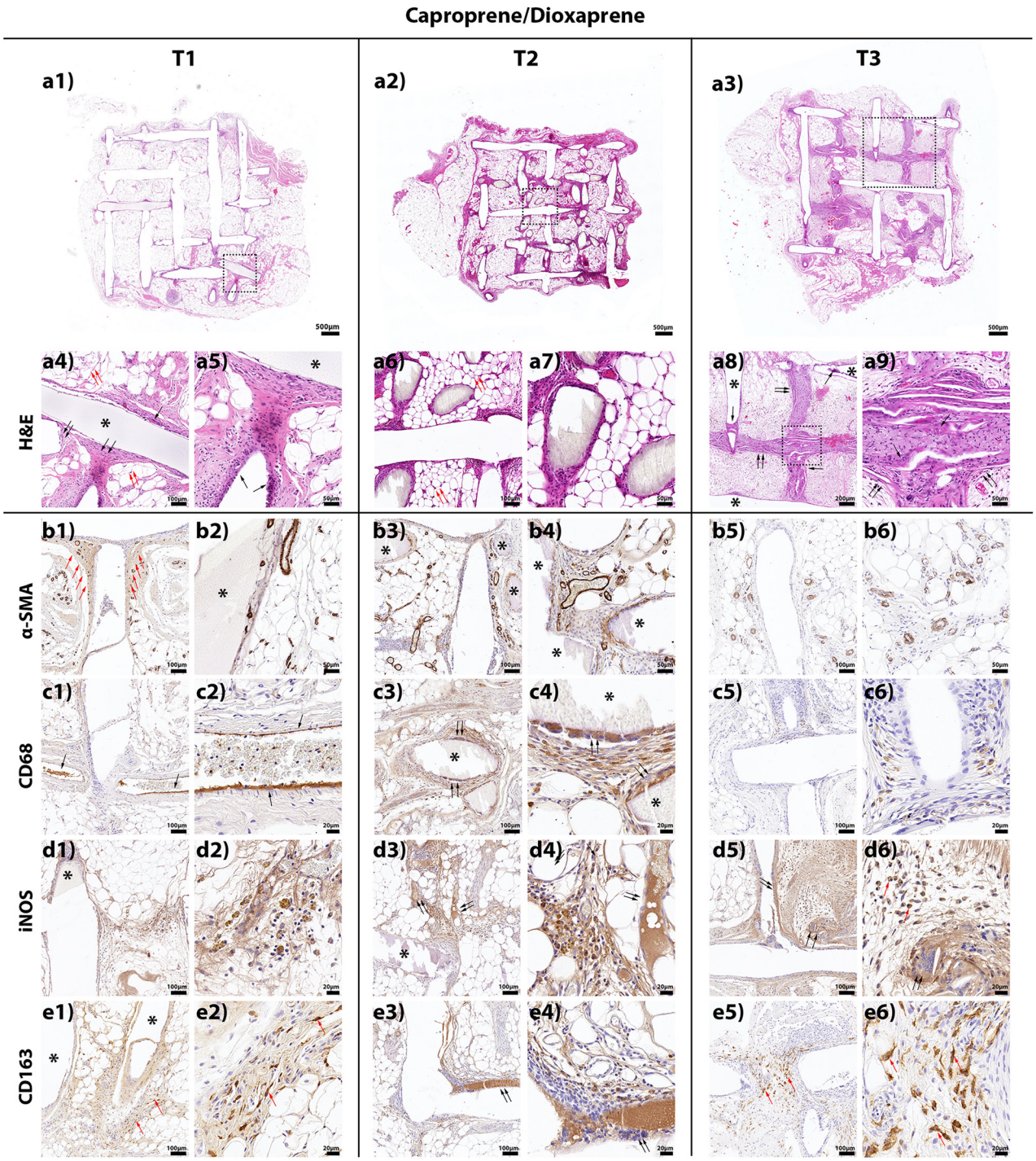

Fig. 9 H&E and immunohistochemical analysis of the CAP/DIO composite at one (T1), three (T2) and six (T3)-month timepoints (n = 5). DIO degradation began at one month (a1), accelerated by three months (a2), and was complete by six months (a3). CAP struts maintained their structure, supporting the newly formed tissue (a1–a3), while DIO strut spaces were replaced by a provisional tissue matrix (a3). At one (a4 and a5) and three (a6 and a7) months, the tissue matrix was mainly adipose tissue within the pore centers (a4 and a6, red arrows) and loose fibrous tissue around the struts (a8 and a9 double black arrows), with giant cells at fusion points (a4 and a5, single black arrows). By six months, DIO was replaced by organized epithelial tissue supported by CAP fibers (a8, dotted square and a9). α-SMA staining showed reactivity at fibrous tissue around the scaffold struts (b1, red arrows), with capillaries forming around struts at one (b1 and b2) and three months (b3 and b4). No fibrous encapsulation was observed by six months (b5 and b6). Positive CD68 reactivity was observed at blood vessels at one month (c1 and c2, black arrows), peaking around degrading DIO at three months (c3 and c4, black arrows), and sharply decreasing by six months (c5 and c6). iNOS activity was present at all timepoints (d1–d6), with the strongest reactivity in fibrous tissue and lymphatic vessels at three months (d3 and d4, double black arrows), decreasing by six months (d5 and d6). iNOS reactivity was also seen at giant cells (d5 and d6, black arrows) and fibroblast/monocyte cells (d6, red arrows). CD163 was observed at fibrous tissue (e1) and fibroblasts (e1 and e2, red arrows) at one month, decreasing and localized at strut edges by three months (e3 and e4, double black arrows). By six months, CD163 was localized to fibroblasts around DIO remnants (e5 and e6, red arrows). Asterisks indicate DIO remnants.

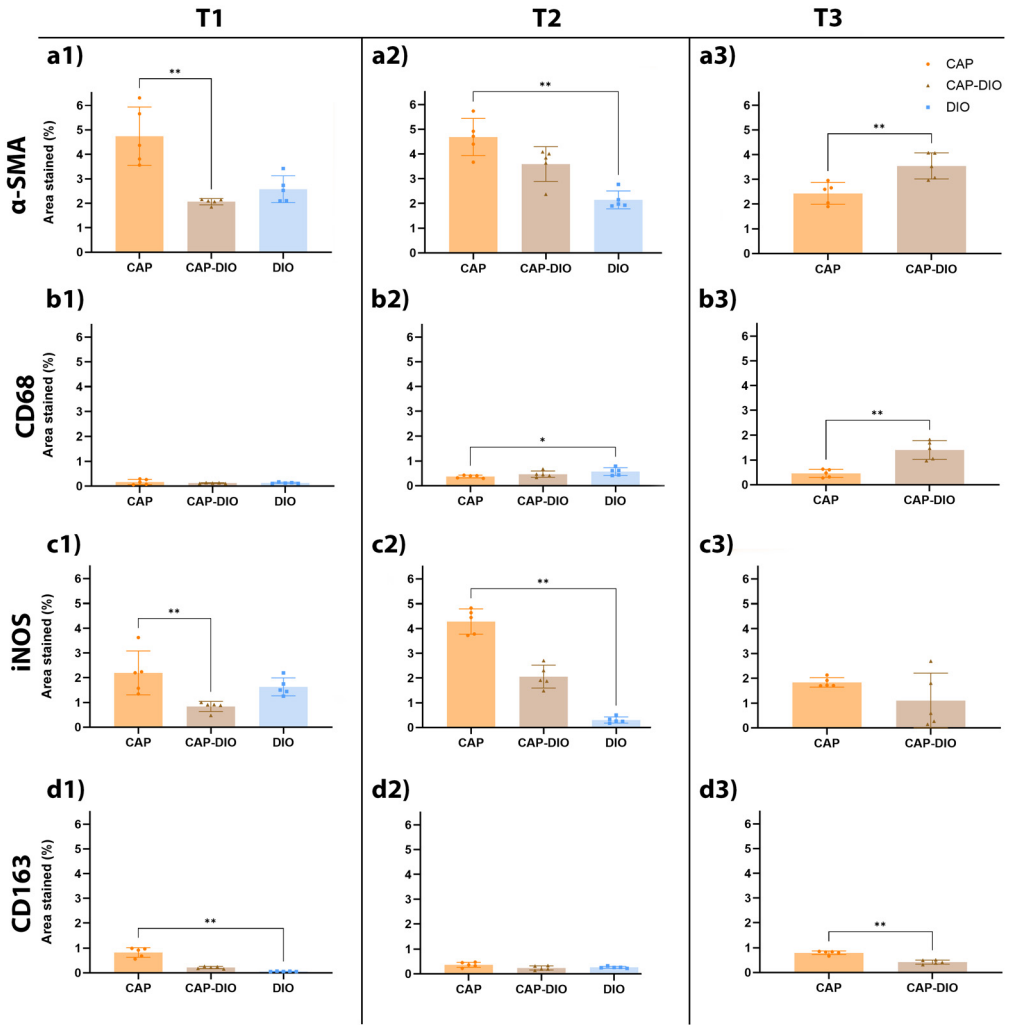

Fig. 10 Quantitative analysis of the immunohistochemical analyses for α-SMA, CD68, iNOS and CD163 markers (n = 5). (a1–a3) The CAP group shows higher α-SMA staining percentages than CAP-DIO and DIO for T1 and T2 timepoints, with significant differences between CAP and CAP-DIO at T1 and CAP and DIO at T2 timepoints. CAP α-SMA expression significantly decreases after six months when compared to the CAP-DIO group; (b1–b3) CD68 staining percentages are generally low across all groups. However, there are significant differences between CAP and DIO at the T2 timepoint and between CAP and CAP-DIO at the T3 timepoint, indicating variations in macrophage activity; (c1–c3) INOS response is characterized by an increasing infiltration of inflammatory cells for the CAP group with significantly higher amounts of iNOS reactivity at T1 and T2 timepoints when compared to CAP-DIO and DIO, respectively. (d1–d3) CD163 staining percentages are relatively low, with significant differences observed mainly at T1 between CAP and DIO, and at T3 between CAP and CAP-DIO groups. The means of the different treatment groups were compared within the same animal and same timepoint. The dataset was analysed using nonparametric Kruskal–Wallis and Mann–Whitney tests. Five tissue sections (n = 5) were used for each antibody (**p < 0.01 and *p < 0.05). Graph bars are depicting the mean with standard deviation.

tinuous cell sheet confining and surrounding the outer surface of the rapidly degrading DIO strut remnants (Fig. 9(c3) and (c4), arrows), possibly scavenging the fast degrading material. Yet, at three months, the provisional matrix tissue formed around the composite struts, especially at CAP fusion points, was also positively stained for CD68 (ESI Fig. S3(c4),† double back arrows). At six months, CD68 macrophagic expression progressively decreased (Fig. 9(c5), (c6) and Fig. S3(c5) and (c6)†).

iNOS expression. At the one-month timepoint, pro-inflammatory immunological activity, detected by iNOS expression, was observed at the loose provisional fibrous tissue formed around the composite struts (Fig. 9(d1), (d2) and Fig. S3(d1) and (d2)†), increasing for the three- and six-month timepoints, especially within the plasma of blood vessels (Fig. 9(d3), (d4) and Fig. S3(d4),† double black arrows) and later at the cell lining and the outer surface of the composite struts (Fig. 9(d5) and Fig. S3(d6),† double back arrows). Positive reactivity of CD68 was also observed at giant cells and fibroblast/monocyte cells within the aggregates of the fibrin strands around the CAP/PDO surface (Fig. 9(d6), red arrows).

CD163 expression. Strong CD163 anti-inflammatory activity was observed within the new provisional tissue formed and fibroblasts at the one-month timepoint (Fig. 9(e1) and (e2), red arrows, and ESI Fig. S3(e1) and (e2),† double back arrows†) and decreasing over the three- and six-month timepoint period. At three months, CD163 expression appeared to be

located around the DIO degrading material and within the plasma of blood vessels closely associated with the outer surface of the construct struts (Fig. 9(e3) and (e4), black arrows, and ESI Fig. S3(e3) and (e4),† black arrows†). Later, at six months, CD163 expression was mainly located at the fibroblast cells of the newly formed fibrous tissue (Fig. 9(e5) and (e6), red arrows, and ESI Fig. S3(e5) and (e6),† double black arrows†).

Complementary quantitative analysis (ESI Fig. S4–S6†) of our qualitative observations indicated that each experimental group triggered a distinct host tissue response, characterized by varying levels of cellular infiltration, vascularization, extracellular matrix deposition, and tissue regeneration. The CAP group exhibited higher α-SMA staining reactivity than both the CAP-DIO and DIO groups, with significant differences emerging between CAP-DIO and DIO at one and three months, respectively (Fig. 10(a1–a3)). Specifically, α-SMA expression in the CAP group significantly decreased after six months compared to the CAP-DIO group (Fig. 10(a3)), with α-SMA primarily localized around blood vessels. This suggests that elevated α-SMA expression was associated with vascular remodeling rather than scaffold encapsulation. In contrast, the DIO group showed increased α-SMA expression at three months, but no encapsulation was observed, as the scaffold material had completely degraded after six months of implantation. CD68 staining, indicating macrophage activity, was generally low across all groups (Fig. 10(b1–b3)); however, significant differences were noted at specific timepoints: between CAP and DIO at three months (Fig. 10(b2)) and between CAP and CAP-DIO at six months (Fig. 10(b3)). Further analysis revealed early inflammatory responses, with the CAP group showing significantly higher iNOS staining compared to CAP-DIO at one month (Fig. 10(c1)) and compared to DIO at three months (Fig. 10(c2)), indicative of a more pronounced M1 macrophage (pro-inflammatory) response at earlier timepoints than after six months (Fig. 10 (c3)). Nevertheless, the CAP group demonstrated consistent signs of constructive tissue remodeling, with significant differences in comparison with the DIO group at one month and in comparison with CAP-DIO at six months (Fig. 10(d1–d3)).

Discussion

This study focused on the design of scaffolds with tuneable dynamic changes in mechanical and structural behaviour critical for SGSTR. The design-dependent workflow allows local tuning of the erosion pathway of the scaffold architecture. It addresses long-term mechanical stability and shape retention to minimize excessive external loads applied to the newly formed tissue at early as well as later stages of regeneration. It also allows modulation of mechanical compliance and free volume expansion, leading to higher compliant deformation due to the regenerated tissue properties. This design concept also yielded a controllable pathway for tissue guidance, resulting in the formation of organized tissue and blood vessels within the expanded pores, which appears to support later stages of mature non-fibrous tissue remodelling.

One notable application of this platform is in developing breast scaffolds, which require large pores due to their size and the extended healing process, often taking over a year for complete tissue regeneration. The platform ensures that these larger pores remain mechanically stable during the later stages of healing while supporting new tissue growth within them. The presence of newly forming tissue within the large pores fosters angiogenesis, encouraging the development of new blood vessels and promoting tissue growth and remodelling throughout the scaffold. This dual functionality is critical for successful long-term regeneration, providing both structural support and an environment conducive to tissue integration and vascularization.

It should be highlighted that the FFF method has significant advantages over pellet-based melt extrusion processes. FFF has the advantage that medical-grade monofilaments of CAP and DIO are exposed to high temperatures for only a short period, namely less than 1 minute. This is especially important for DIO since it is sensitive to thermal degradation, leading to highly compromised melt processing over time.[18]

Importantly, from a translational research point of view, utilizing FFF along with medical-grade polymers facilitates regulatory considerations in scaffold design, material selection, and manufacturing to fulfil quality system (QS) requirements and enhance the study's suitability for a future regulatory approval process.[19]

In the study's first phase, we investigated which accelerated degradation conditions mimic the physiological erosion pathway that occurs *in vivo* at pH 7. *In vivo*, the degradation of aliphatic polyesters predominantly proceeds through hydrolysis of the polymer backbone rather than through enzymatic degradation.[20] However, since *in vitro* degradation of some polyesters at ~pH 7 occurs over an extended period, acid- or base-catalysed hydrolysis is widely used by researchers to accelerate the *in vitro* degradation process.[21,22] It is hypothesized that *in vitro* accelerated degradation exhibits degradation pathway(s) and mechanical changes that predict those observed in a physiological environment.

The results of this study suggested that both DIO and CAP exhibit bulk erosion in acidic and neutral environments and show severe surface erosion under basic conditions. This difference is attributed to different water penetration rates and hydrolysis speeds for these media. The degradation kinetics of polyesters is governed by the hydrolytic cleavage of ester bonds on the polymer backbone. Under basic conditions, since hydrolysis is faster than water penetration, hydrolytic attack mainly occurs on the surface of the polymer. Meanwhile, under acidic and neutral conditions, water penetrates the polymer faster than hydrolytic attack on the surface and thus hydrolysis internally within the polymer network leads to predominantly bulk degradation.[23] Therefore, compared to basic conditions, acidic and neutral conditions result in similar changes in mass, morphology, crystallinity, thermal behaviour, mechanical properties and stability of the structures, albeit over a faster time course under acidic conditions.

In most of the previously published studies, accelerated hydrolytic degradation of polyesters has been performed under

basic conditions, likely due to the more aggressive hydrolysis reaction than acid catalysis.[24,25] However, the results herein show that acid catalysis closely mirrors the erosion pathway under neutral conditions and therefore is better suited as a degradation model than the frequently used basic model. This is an important finding, with implications across various study designs. Accelerated degradation is a valuable tool for studying the behaviour of materials with long periods of degradation under physiological conditions. Rather than replacing the need for real-time degradation studies, accelerated degradation provides a complementary approach that can answer some preliminary questions and hence aid in the design of longer-term studies. Thus, using an accelerated model that mimics the changes observed under neutral conditions as closely as possible is imperative.

In most previous studies, polydioxanone and polycaprolactone, the main components of DIO and CAP, have been investigated in films.[26,27] Yet, it has been observed that for 3D-printed structures, loss of integrity is mainly prominent at the fusion points where cracks or small contact areas result in delamination and failure.[4] It is therefore imperative to assess the modes and degradation kinetics of 3D-printed scaffolds, rather than bulk or cast materials, because, for scaffolds, failure is primarily due to degradation at the fusion points.

In the next phase of the study, utilizing toolpath planning and multi-material printing, composite scaffolds of CAP/DIO were developed and evaluated under accelerated degradation. Over six hours of degradation in acidic media (corresponding to 7–8 weeks under neutral conditions), SEM analysis illustrated that DIO struts became highly fragile and disintegrated. In contrast, CAP struts remained stable at the fusion points. During this time, the pore size increased and the structure indicated a more flexible and compliant behaviour while long-term integrity was preserved. CAP/DIO composite scaffolds with aspect ratios of 1 : 1 and 1 : 2 indicated a 2.1-fold and 3.1-fold reduction in elastic modulus, respectively, while the pore size increased from 0.5 to 2 mm and 1 to 2 mm, respectively. This result demonstrates that by using different design strategies for CAP and DIO struts, the erosion pathway of the composites and changes in their mechanical and structural characteristics can be modulated, where degradation of DIO produces larger pores and increased mechanical compliance while the stability of CAP fusion points provides long-term integrity.

In vivo biocompatibility is a critical characteristic of a 3D scaffold printed from a medical-grade polymer. To study the *in vivo* degradation and biocompatibility, single-material and dual-material scaffolds were implanted subcutaneously in rats for six months. The DIO single-material scaffold demonstrated the fastest degradation rate with a rapid reduction in elastic modulus from 7.82 to 0.03 MPa after three months and complete disintegration after six months. In contrast, the CAP single-material scaffold preserved its structural integrity, showing an increased elastic modulus from 5.58 to 6.92 MPa and an increasing trend towards a brittle structure. These results align with other studies, showing that the amorphous phase is degraded first, leading to an overall higher crystallinity of the remaining macromolecular scaffold architecture.[26,27]

The surgical trauma associated with the preparation of the implant site initiates a cascade of physiological processes that comprise wound healing. The surgery to implant the scaffolds initially induces a vascular response in intact vessels surrounding the implant site, resulting in the leakage of fluid (edema) and blood proteins. Blood elements from the cut vessels form a fibrin clot, a provisional matrix into which cells can migrate. Phagocytic cells, first polymorphonuclear neutrophils and then macrophages, infiltrate the surgical site and begin ingesting the cellular and extracellular matrix debris. Endothelial cell migration and the formation of new blood vessels follow. Fibroblasts invade the fibrin clot and form an extracellular matrix mainly composed of types I and III collagen. The tissue comprising phagocytic cells, newly forming blood vessels and fibroblasts, which form within the first days (acute phase) of healing, is referred to as granulation tissue. After that, the parenchymal cells of the surrounding tissue begin to infiltrate the newly forming stroma. H&E analysis of DIO scaffolds demonstrated that the provisional matrix initially starts to form around the surface of the struts. However, after three months, the morphology was totally subsided and left with disorganized loose collagen fibers that could not retain the shape of the original architecture. The remnants of DIO were also surrounded by multinuclear cells, representing the last stages of a foreign body reaction.

Conversely, H&E analysis of CAP scaffolds indicated that the fibers and pore size remained stable up to six months post-implantation, and thick collagen fibers were formed around the fusion points. No sign of fibrotic encapsulation was observed for both DIO and CAP scaffolds. Moreover, significant longitudinal differences between M1 and M2 macrophagic activity were quantitatively detected. There appeared to be simultaneous pro-inflammatory and anti-inflammatory activity highly expressed at the surface of the DIO and CAP struts, as well as within the provisional matrix formed, possibly due to the body's attempt to degrade/remove the CAP and DIO remnants as well as regulate the angiogenesis processes. The interplay between α-SMA and iNOS expression patterns reinforces this observation. Since iNOS has been associated with vascular remodeling,[28,29] its expression aligns with α-SMA expression at blood vessels observed at later timepoints. Macrophages play a crucial role in this process, releasing vascular endothelial growth factor signals that drive vessel recruitment. Sprouting endothelial cells and fibroblasts follow these cues and orchestrate extracellular matrix deposition. Consistent with previous studies using similar materials, M1 activity was significantly greater than M2 activity in the CAP and CAP-DIO groups over the first three months. However, this disparity became less pronounced after six months.[30] These observations confirm the coexistence of both macrophage subtypes and emphasize their critical role in scaffold degradation, integration and vascular and tissue remodelling at later stages of SGSTR.

The erosion and tissue formation pathways of CAP/DIO scaffolds differed significantly from those of single-material scaffolds of DIO and CAP. The dual material scaffolds remained mechanically stable after six months of implantation while showing a gradual decrease in the elastic modulus from 5.84 to 2.84 MPa (increase in compliance) and, at the same time, showing a 2-fold increase in pore size (expansion of free volume). Remarkably, H&E results demonstrated that DIO struts were entirely replaced with a continuous provisional stroma-like highly organized and vascularized tissue. The newly formed tissue was mechanically supported by CAP struts and retained its shape and integrity, while following the overall geometry of the scaffold. This guided tissue regeneration pathway observed in the CAP/DIO composite results from the locally tailored erosion pathway, attributed to the rational contribution of slow and fast degrading polymers in the composite structure. Initially, DIO struts provide a high surface area, facilitating cell attachment and proliferation. They act as a guide for forming the fibrin clot and subsequently for hosting cells while gradually degrading to provide larger local spaces for the invading tissue. Since the newly formed tissue is mechanically supported by CAP struts, it does not collapse, even after the disintegration of DIO struts. Instead, it results in a highly structured stroma-like tissue after six months. Such a well-ordered tissue formation was not observed in single-material scaffolds of CAP or DIO. Thus, it appears that the presence and interplay of both polymers are essential in the guided tissue regeneration pathway from early stages of cell attachment to later regeneration and remodelling stages.

Conclusion

Rational design strategies for CAP and DIO struts using toolpath planning of multi-nozzle 3D printers offer a promising approach to modulate the biodegradation and mechanical properties of a dual-material scaffold for SGSTR. This approach allows for increased mechanical compliance, expansion of free volume, and improved mechanical stability and shape retention for up to six months, which are critical requirements for SGSTR. These controllable mechanical and architectural variations result in the formation of highly organized and vascularized soft tissue. Additionally, through polymer degradation, enlarged pores are formed, which support further stages of angiogenesis and stroma tissue formation.

Author contributions

Mina Mohseni: conceptualization, data curation, methodology, analysis, and writing – original draft; Silvia Cometta: data curation and writing & editing; Leopold Klein: data curation and analysis; Marie-Luise Wille: data curation; Cedryck Vaquette: data curation and methodology; Dietmar W. Hutmacher: conceptualization, funding acquisition, resources, supervision, and writing & editing; Flavia Medeiros Savi: data curation, analysis, and writing – original draft.

Data availability

Data for this article are available at Research Data Finder provided by Queensland University of Technology at **https://doi.org/10.25912/RDF_1723555435721**.

Conflicts of interest

There are no conflicts to declare.

Acknowledgements

This work was supported by the Australian Research Council (DP230102934) and ARC Industrial Transformation Training Centre for Multiscale 3D Imaging, Modelling, and Manufacturing (IC 180100008), NHMRC 2008018 – Transformation of the implant paradigm in breast rehabilitation grant and the Max Planck Queensland Centre.

References

1 J. Henkel, *et al.*, Bone regeneration based on tissue engineering conceptions—a 21st century perspective, *Bone Res.*, 2013, **1**, 216.
2 M. Mohseni, *et al.*, Adipose tissue regeneration: Scaffold—Biomaterial strategies and translational perspectives, in *Biomaterials in Translational Medicine*, Elsevier, 2019, p. 291–330.
3 M. Lu, *et al.*, 3D printed porous PLGA/n-HA/MgP composite scaffolds with improved osteogenic and angiogenic properties, *Mater. Des.*, 2023, **234**, 112351.
4 M. Mohseni, D. W. Hutmacher and N. J. Castro, Independent evaluation of medical-grade bioresorbable filaments for fused deposition modelling/fused filament fabrication of tissue engineered constructs, *Polymers*, 2018, **10**(1), 40.
5 C. Culmone, G. Smit and P. Breedveld, Additive manufacturing of medical instruments: A state-of-the-art review, *Addit. Manuf.*, 2019, 461–473.
6 Q. Yan, *et al.*, A review of 3D printing technology for medical applications, *Engineering*, 2018, **4**(5), 729–742.
7 M. Javaid and A. Haleem, Additive manufacturing applications in medical cases: A literature based review, *Alexandria J. Med.*, 2018, **54**(4), 411–422.
8 N. Sears, *et al.*, Fabrication of biomimetic bone grafts with multi-material 3D printing, *Biofabrication*, 2017, **9**(2), 025020.
9 S. M. Bittner, *et al.*, Fabrication and mechanical characterization of 3D printed vertical uniform and gradient scaffolds for bone and osteochondral tissue engineering, *Acta Biomater.*, 2019, **90**, 37–48.

10 L. Diaz-Gomez, *et al.*, Multimaterial segmented fiber printing for gradient tissue engineering, *Tissue Eng., Part C*, 2019, **25**(1), 12–24.
11 B. T. Smith, *et al.*, Multimaterial Dual Gradient Three-Dimensional Printing for Osteogenic Differentiation and Spatial Segregation, *Tissue Eng., Part A*, 2019, 239–252.
12 J. Liu, *et al.*, 3D printing of biomimetic multi-layered GelMA/nHA scaffold for osteochondral defect repair, *Mater. Des.*, 2019, **171**, 107708.
13 M. G. Flores, *et al.*, Periodontal ligament cell sheet promotes periodontal regeneration in athymic rats, *J. Clin. Periodontol.*, 2008, **35**(12), 1066–1072.
14 A. Limaye, Drishti: a volume exploration and presentation tool, in *Developments in X-ray Tomography VIII*, International Society for Optics and Photonics, 2012.
15 D. S. Sparks, *et al.*, A preclinical large-animal model for the assessment of critical-size load-bearing bone defect reconstruction, *Nat. Protoc.*, 2020, **15**(3), 877–924.
16 F. Medeiros Savi, *et al.*, A new automated histomorphometric MATLAB algorithm for immunohistochemistry analysis using whole slide imaging, *Tissue Eng., Part C*, 2020, **26**(9), 462–474.
17 T. J. Hinton, *et al.*, Three-dimensional printing of complex biological structures by freeform reversible embedding of suspended hydrogels, *Sci. Adv.*, 2015, **1**(9), e1500758.
18 S. Luposchainsky, *et al.*, Melt Electrowriting of Poly (dioxanone) Filament Using a Multi–Axis Robot, *Macromol. Mater. Eng.*, 2022, **307**(12), 2200450.
19 S. B. Stiansen, Defining the standard for medical grade polymers, 2018, Available from: **https://www.medicalplasticsnews.com/medical-plastics-industry-insights/what-is-a-medical-grade-polymer/**.
20 M. Therin, *et al.*, In vivo degradation of massive poly (α-hydroxy acids): validation of in vitro findings, *Biomaterials*, 1992, **13**(9), 594–600.
21 G. P. Sailema-Palate, *et al.*, A comparative study on Poly (ε-caprolactone) film degradation at extreme pH values, *Polym. Degrad. Stab.*, 2016, **130**, 118–125.
22 M. Bartnikowski, *et al.*, Degradation mechanisms of polycaprolactone in the context of chemistry, geometry and environment, *Prog. Polym. Sci.*, 2019, 1–20.
23 G. P. Sailema-Palate, *et al.*, A comparative study on Poly (ε-caprolactone) film degradation at extreme pH values, *Polym. Degrad. Stab.*, 2016, **130**, 118–125.
24 S.-H. Lee, *et al.*, Analysis of degradation rate for dimensionless surface area of well-interconnected PCL scaffold via *in vitro* accelerated degradation experiment, *Tissue Eng. Regener. Med.*, 2014, **11**(6), 446–452.
25 P. S. Poh, *et al.*, Data for accelerated degradation of calcium phosphate surface-coated polycaprolactone and polycaprolactone/bioactive glass composite scaffolds, *Data Brief*, 2016, **7**, 923–926.
26 M. A. Sabino, *et al.*, Study of the hydrolytic degradation of polydioxanone PPDX, *Polym. Degrad. Stab.*, 2000, **69**(2), 209–216.
27 C. Ping Ooi and R. E. Cameron, The hydrolytic degradation of polydioxanone (PDSII) sutures. Part I:Morphological aspects, *J. Biomed. Mater. Res.*, 2002, **63**(3), 280–290.
28 H. Kleinert and U. Forstermann, Inducible Nitric Oxide Synthase, in*xPharm: The Comprehensive Pharmacology Reference*, Elsevier Inc., Amsterdam, The Netherlands, 2007.
29 K. E. Martin and A. J. García, Macrophage phenotypes in tissue repair and the foreign body response: Implications for biomaterial-based regenerative medicine strategies, *Acta Biomater.*, 2021, **133**, 4–16.
30 R. Finze, *et al.*, Histological and Immunohistochemical Characterization of Osteoimmunological Processes in Scaffold-Guided Bone Regeneration in an Ovine Large Segmental Defect Model, *Biomedicines*, 2023, **11**(10), 2781.